Supporting Information: Structure, energetics, and spectra for the oxygen vacancy in rutile: prominence of the Ti-H_O-Ti bond

William R. Palfey[a], George R. Rossman[a,], William A Goddard III[b,]**

[a]Division of Geological and Planetary Sciences, California Institute of Technology, Pasadena, CA, USA

[b]Materials and Process Simulation Center (MSC), MC 139-74, California Institute of Technology, Pasadena CA, 91125, USA

* To whom correspondence is to be addressed: wag@caltech.edu; grr@caltech.edu

ORCID: WAG) 0000-0003-0097-5716; WP, GRR 0000-0002-4571-6884

TABLE OF CONTENTS

Summary of 1H defect relaxations……S3

Summary of 2H defect relaxations……...…….S4

Model of all relaxed H positions……..…….S5

Charge and spin density plots……...……...…S6-S8

Bader charge analyses, H_i……...……...……S9

Bader charge analyses, H_O……...……S10

Select density of states and band structures……...……..S11-S14

Summary of all calculated H modes……...…….S15-S16

Additional commentary on mode calculations…….S17-S18

Heat of formation calculations……...……..S19

Accuracy of PBE-D3 level of DFT……...S20

Table S1. The energies, hydrogen bonding distances and hydrogen bond angles for all 21 of the single H defects. Ending positions of "H_i" are all CC oriented.

Defect site	Final H position	Total energy (eV)	d(OH···O) (Å)	Ti-O-H angle
H_{A2}	H_O	-432.066	N/A	N/A
H_{K2}	H_i	-430.647	2.95	173.0
H_{D3}	H_i	-430.629	2.83	174.3
H_{M2}	H_i	-430.623	2.95	173.2
H_{E4}	H_i	-430.577	2.91	172.7
H_{G3}	H_i	-430.550	2.83	172.8
H_{J3}	H_i	-430.539	2.96	172.0
H_{H4}	H_i	-430.501	2.90	171.7
H_{F3}	H_i	-430.489	2.97	172.4
H_{J4}	H_i	-430.488	3.21	168.3
H_{B2}	H_i	-430.484	3.00	173.4
H_{I3}	H_i	-430.478	3.01	171.4
H_{H3}	H_i	-430.47	3.08	171.3
H_{F4}	H_i	-430.443	2.96	172.4
H_{I4}	H_i	-430.44	2.95	175.7
H_{E3}	H_i	-430.385	N/A	N/A
H_{D4}	H_i	-430.374	2.88	164.4
H_{G4}	H_i	-430.37	2.96	170.1
H_{C2}	H_i	-430.295	2.94	173.1
H_{L2}	H_i	-430.238	2.96	175.2
H_{N2}	H_i	-430.187	2.95	172.9

Table S2. The energies, hydrogen bonding distances, hydrogen bond angles and average Ti-H distances for all 21 of the two H defects. Ending positions of "H_i" are all CC oriented.

Defect sites	Final H positions	Total energy (eV)	d(OH···O) (Å)	Avg. Ti-H (Å)	Ti-O-H angle
H_{A2}, H_{M2}	H_O, H_i	-435.093	2.94	2.04	173.1
H_{A2}, H_{E4}	H_O, H_i	-435.085	2.91	2.03	173.1
H_{A2}, H_{K2}	H_O, H_i	-435.084	2.96	2.03	173.4
H_{A2}, H_{G3}	H_O, H_i	-435.074	2.83	2.04	174.9
H_{A2}, H_{D3}	H_O, H_i	-435.070	2.81	2.04	173.6
H_{A2}, H_{F3}	H_O, H_i	-435.041	2.95	2.04	172.8
H_{A2}, H_{I3}	H_O, H_i	-435.037	2.89	2.03	173.5
H_{A2}, H_{J3}	H_O, H_i	-435.023	2.92	2.04	173.1
H_{A2}, H_{H4}	H_O, H_i	-435.017	2.92	2.03	173.4
H_{A2}, H_{J4}	H_O, H_i	-435.015	3.04	2.04	171.4
H_{A2}, H_{B2}	H_O, H_i	-435.000	2.91	2.04	173.6
H_{A2}, H_{D4}	H_O, H_i	-434.961	2.97	2.03	169.5
H_{A2}, H_{G4}	H_O, H_i	-434.959	2.91	2.04	174.0
H_{A2}, H_{L2}	H_O, H_i	-434.856	2.90	1.96	173.0
H_{A2}, H_{N2}	H_O, H_i	-434.839	2.89	1.98	173.2
H_{A2}, H_{C2}	H_O, H_i	-434.797	2.84	1.97	175.8

Defect sites	Final H positions	Total energy (eV)	d(OH···O) 1 (Å)	d(OH···O) 2 (Å)	Ti-O-H angle 1	Ti-O-H angle 2
H_{D3}, H_{M2}	H_i, H_i	-433.671	2.82	2.83	176.1	174.8
H_{K2}, H_{G3}	H_i, H_i	-433.588	2.91	2.94	173.1	171.6
H_{D3}, H_{K2}	H_i, H_i	-433.579	2.87	2.99	175.3	172.6
H_{D3}, H_{G3}	H_i, H_i	-433.491	2.61	2.75	170.7	173.0

Defect sites	Final H positions	Total energy (eV)	d(OH···O) (Å)	Avg. Ti-H (Å)	Ti-O-H angle
H_{K2}, H_{M2}	H_i, H_{alt}	-432.258	3.03	1.81	171.7

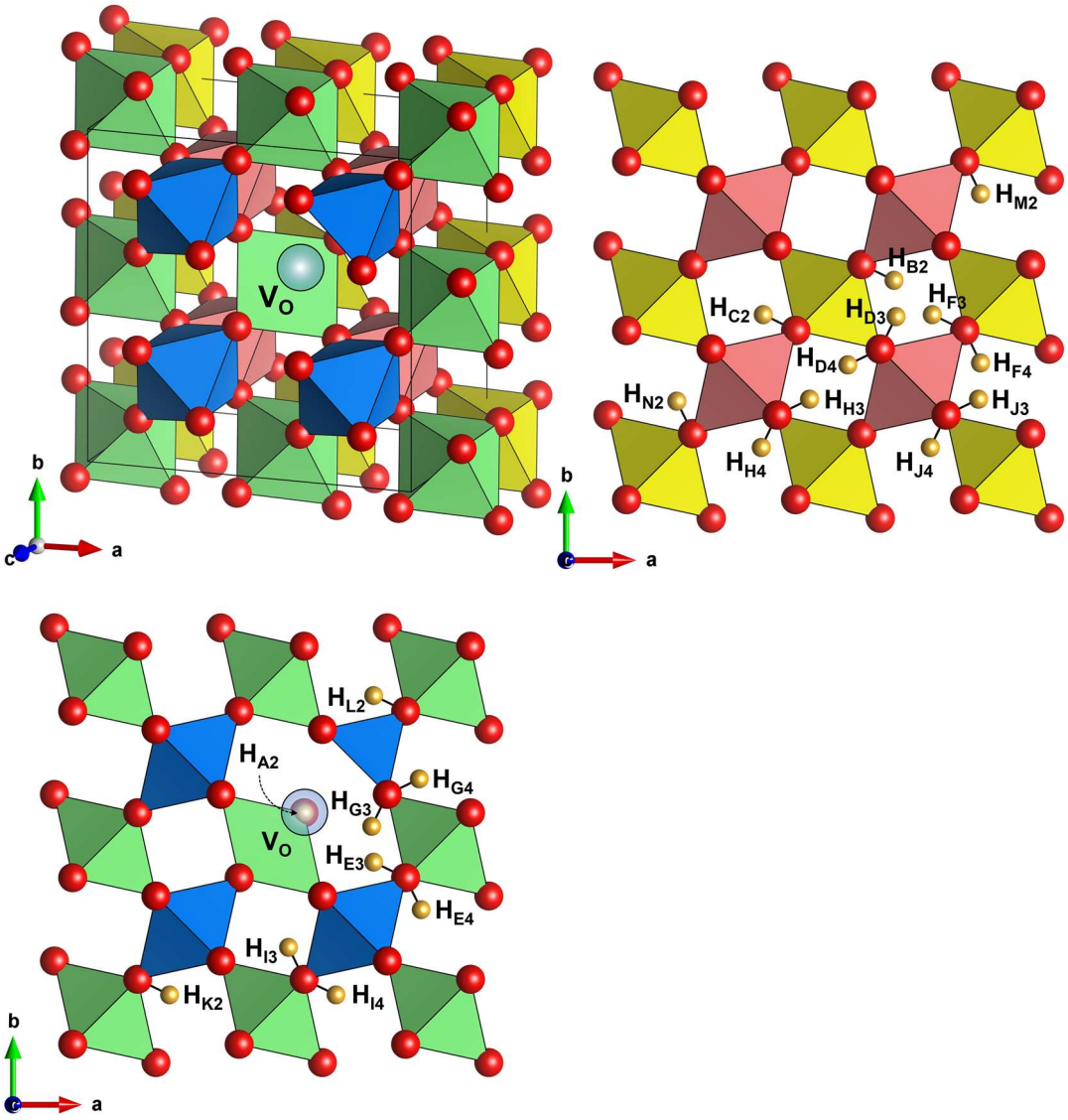

Figure S1. Comprehensive summary of the O vacancy structure and H positions from fully relaxed structures with one O vacancy and one added H. Octahedral Ti sites are color coded by layer in the c-direction. O atoms are represented by red spheres, H atoms by bronze spheres, and the O vacancy (VO) by a transparent blue sphere. All OH-bonds are in a channel-centered orientation. Upon structural relaxation, H starting in the A2 position moves to the O vacancy, rather than forming an OH bond. All 21 final positions for H are presented. There are four layers ordered in the c direction: gold, red, green, and blue in sequence. The O vacancy is in the blue layer.

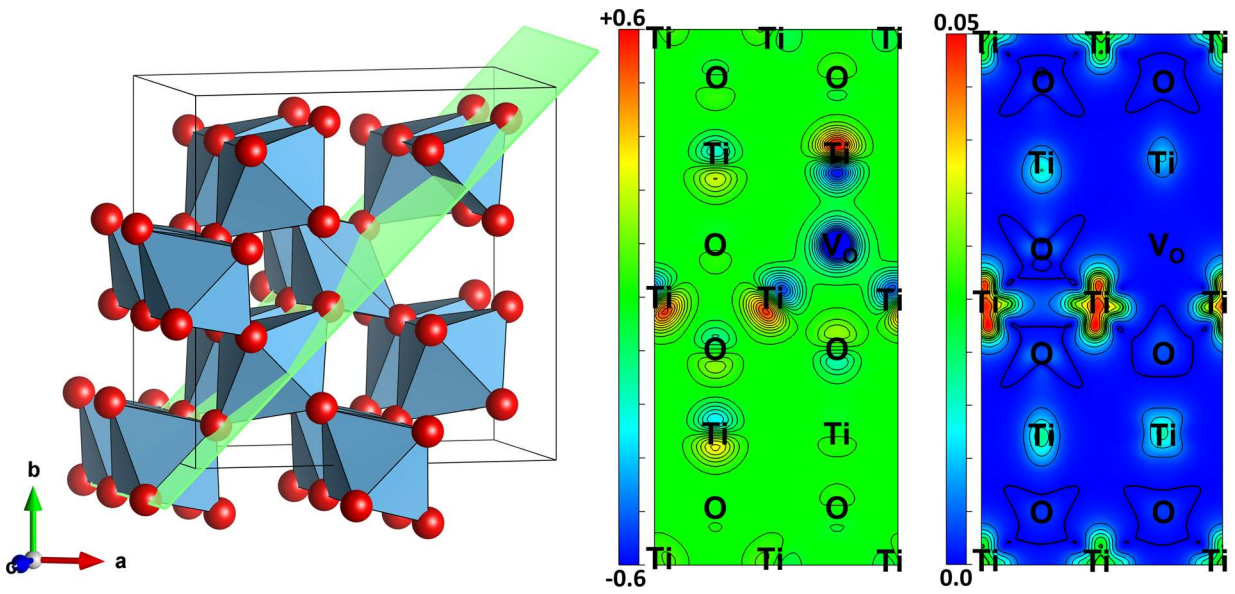

Figure S2. Charge and spin densities for the O vacancy system with no added H. Left: the (-110) plane, over which the charge and spin densities are plotted, is highlighted in green. Center: The charge density difference between the O vacancy structure and a perfect rutile crystal. A significant loss of charge is attributed to the O vacancy. Right: The absolute value spin density for the O vacancy structure. Despite similar changes in charge between the three Ti atoms surrounding the O vacancy, the unpaired spin is mostly limited to the two atoms adjacent in the c direction. The shape of the spin density surrounding these Ti atoms suggests occupation of the dxy orbital. Additionally, some unpaired spin is predicted to occupy Ti atoms further away from the O vacancy, also adjacent in the c direction.

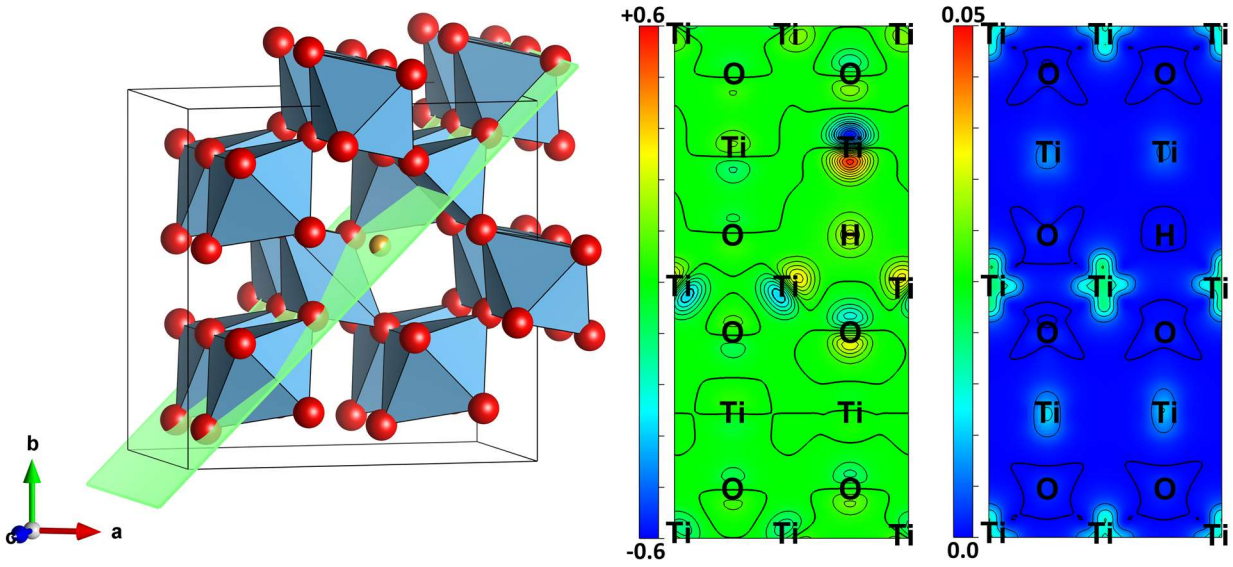

Figure S3. Charge and spin densities for the H_O defect for the case of one H added to the O vacancy structure. **Left:** the (-110) plane, over which the charge and spin densities are plotted, is highlighted in green. **Center:** The charge density difference between the H_O and O vacancy structure. As expected, there is an increase in charge associated with the inclusion of H. Of the three Ti atoms surrounding H_O, the one furthest away experiences the greatest net increase in charge, while the two closer Ti atoms experience a relatively modest charge increase. **Right:** The absolute value spin density for the H_O structure. Similar to the O vacancy structure, most of the unpaired spin is on the two Ti atoms adjacent in the c direction, while virtually none is associated with the third H-adjacent Ti atom. This shows the bonding between H_O and the two adjacent Ti atoms in the c-direction.

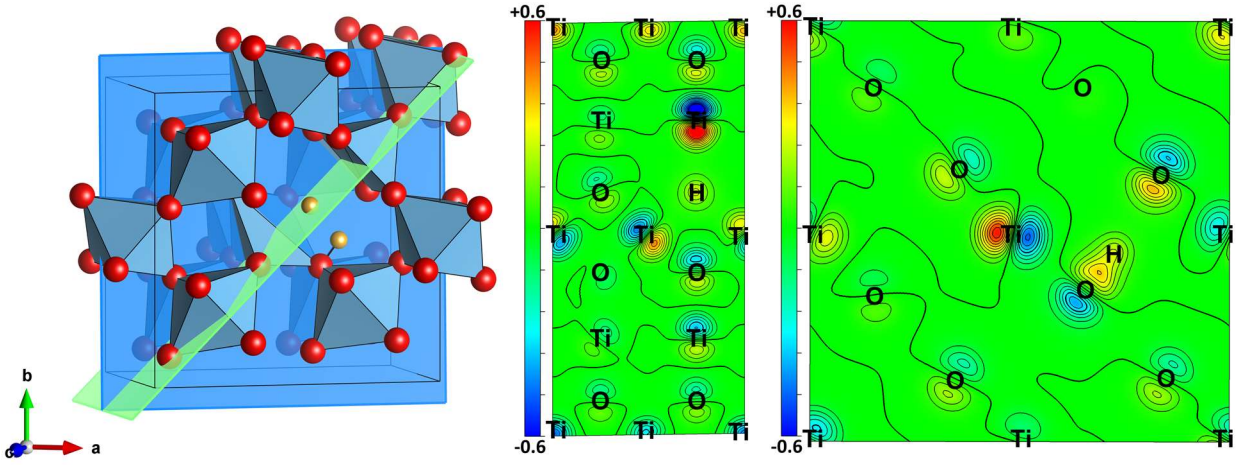

Figure S4. Two H added to O vacancy structure. Charge densities for the H_O defect and OH in the 2H system with the OH bond at the D3 site. Spin density plots are not presented, as virtually no unpaired spin was predicted in these systems. Left: The (-110) and plane (green) and (002) plane (blue), over which the charge density differences have been plotted. Center: The charge density difference in the plane of H_O and its surrounding Ti atoms. The charge distribution is largely similar to the single H_O case. Right: The absolute value spin density is plotted to highlight the charge densities associated with the OH bond. A continuous positive charge volume exists between H and its bonded O, revealing the covalent character of the OH bond. This is in stark contrast with H_O in the same structure.

Table S3. Results of Bader charge analyses for the H_i positioned hydrogen atom in the 2H defects. Both the charge values and Bader volumes are significantly lower than for H_O, consistent with the formation of OH.

Defect Sites	H_i Charge	H_i Volume (Å^3)
H_{A2}, H_{M2}	0.356	1.345
H_{A2}, H_{E4}	0.375	1.359
H_{A2}, H_{K2}	0.369	1.375
H_{A2}, H_{G3}	0.364	1.310
H_{A2}, H_{D3}	0.366	1.288
H_{A2}, H_{F3}	0.354	1.309
H_{A2}, H_{I3}	0.372	1.347
H_{A2}, H_{J3}	0.371	1.342
H_{A2}, H_{H4}	0.380	1.378
H_{A2}, H_{J4}	0.393	1.476
H_{A2}, H_{B2}	0.361	1.304
H_{A2}, H_{D4}	0.390	1.440
H_{A2}, H_{G4}	0.372	1.353
H_{A2}, H_{L2}	0.364	1.327
H_{A2}, H_{N2}	0.370	1.327
H_{A2}, H_{C2}	0.360	1.281
AVERGE	0.370	1.348

Table S4. Results of Bader charge analyses for the H_O positioned hydrogen atom in the 2H defects and H_{A2}. Both the charge values and Bader volumes are significantly higher than for H_i, consistent with anionic hydrogen.

DEFECT	H_O CHARGE	H_O VOLUME (Å^3)
H_{A2}, H_{M2}	1.571	8.157
H_{A2}, H_{E4}	1.578	8.126
H_{A2}, H_{K2}	1.572	8.061
H_{A2}, H_{G3}	1.569	7.868
H_{A2}, H_{D3}	1.563	7.891
H_{A2}, H_{F3}	1.579	8.203
H_{A2}, H_{I3}	1.575	8.174
H_{A2}, H_{J3}	1.570	8.126
H_{A2}, H_{H4}	1.572	8.131
H_{A2}, H_{J4}	1.572	8.179
H_{A2}, H_{B2}	1.567	8.235
H_{A2}, H_{D4}	1.574	8.247
H_{A2}, H_{G4}	1.580	8.403
H_{A2}, H_{L2}	1.573	7.595
H_{A2}, H_{N2}	1.578	7.800
H_{A2}, H_{C2}	1.573	7.746
H_{A2}	1.567	8.174
AVERAGE	1.573	8.066

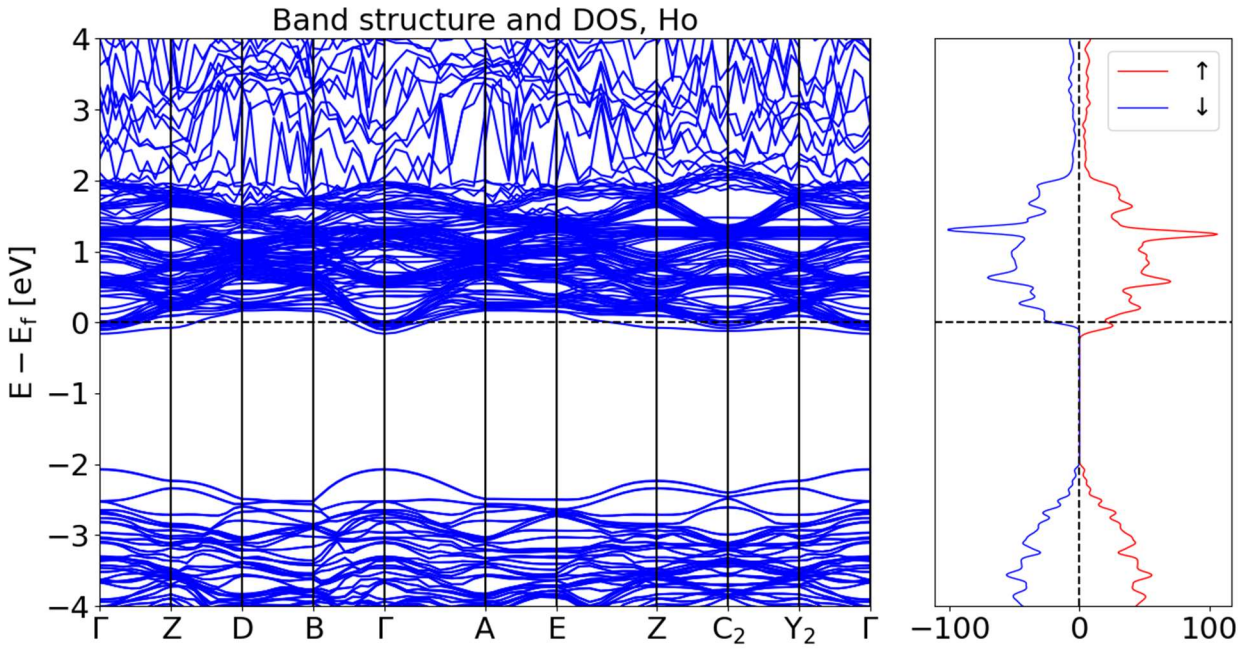

Figure S5. Band structure (left) and density of states (right) for the single hydrogen, H_O defect (H_{A2} case). Note the states and unpaired spin present just below the Fermi energy. This is attributed to the excess electrons resulting from V_O which have been delocalized across Ti atoms throughout the structure. The largest portion of the unpaired spin and excess charge is confined to the two Ti atoms bonded to H_O.

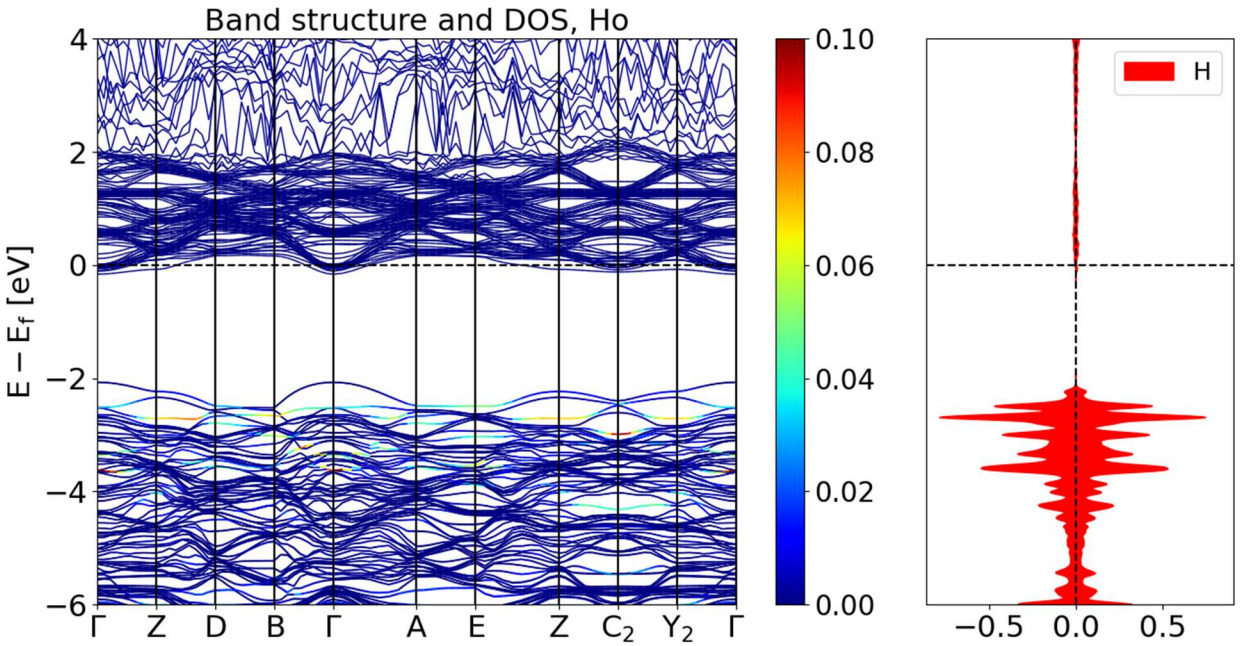

Figure S6. Band structure (left) and density of states (right) for the single hydrogen, H_O defect (H_{A2} case). Only the states attributed to H are plotted on the right, and the corresponding bands are highlighted on the left, with warmer colors indicating higher levels of occupation. The Ti_{dxy}-H_s-Ti_{dxy} to Ti_{dxy}-Ti_{dxy} transition is measured from the highest H band to the Ti bands present just below the Fermi energy.

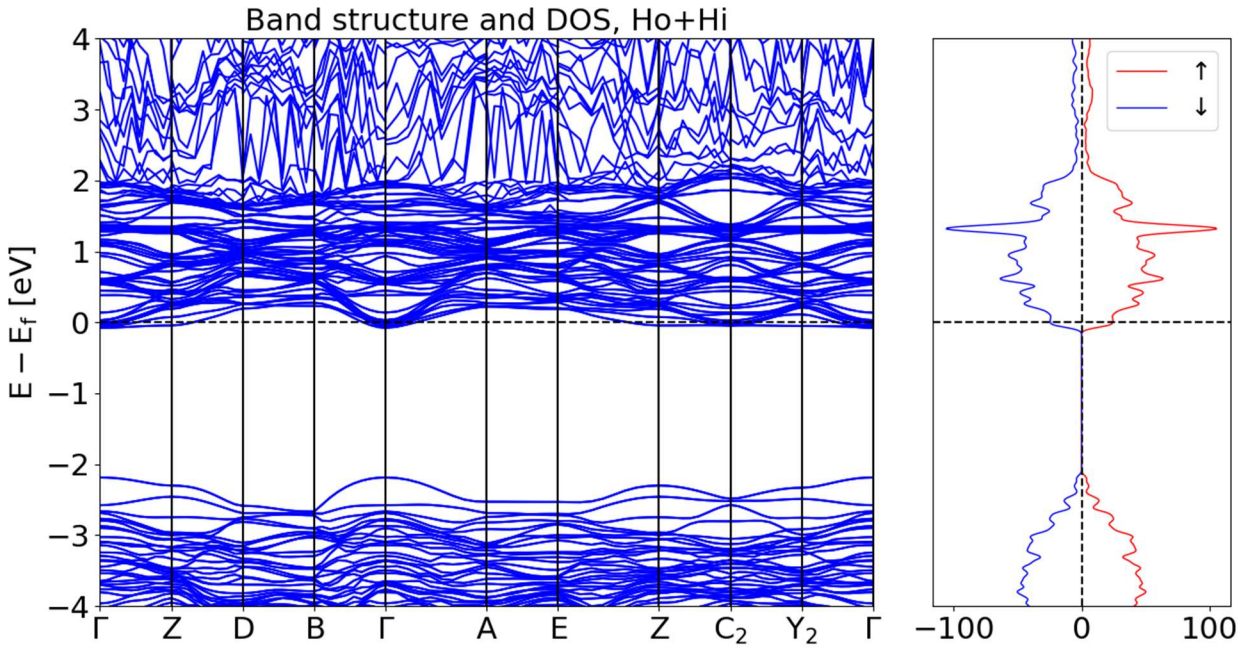

Figure S7. Band structure (left) and density of states (right) for the two hydrogen, H_O + H_i defect system (H_{A2}, H_{M2} case). Note the states present just below the Fermi energy, similar to the single hydrogen case. However, in contrast to the single hydrogen case, this system has no unpaired spins. The largest portion of the excess charge resulting from V_O is confined to the two Ti atoms bonded to H_O, with the remained being delocalized across other Ti pairs.

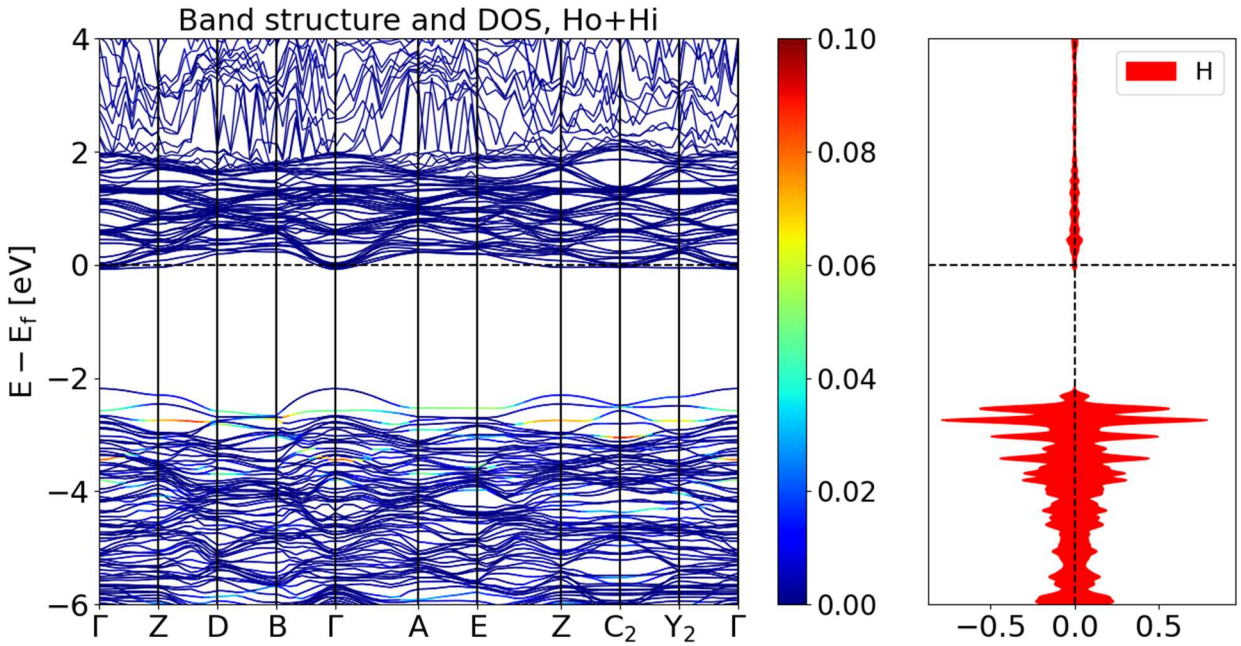

Figure S8. Band structure (left) and density of states (right) for the two hydrogen, H_O + H_i defect system (H_{A2}, H_{M2} case). Only the states attributed to H are plotted on the right, and the corresponding bands are highlighted on the left, with warmer colors indicating higher levels of occupation. The Ti_{dxy}-H_s-Ti_{dxy} to Ti_{dxy}-Ti_{dxy} transition is again measured from the highest H band to the Ti bands present just below the Fermi energy, similar to the single hydrogen case.

Table S5. All calculated H-associated vibrational modes are presented above. Emphasis was placed on calculating modes for either structures with unusual geometries (i.e. short or long bond lengths) or the lowest energy structures (i.e. those with Boltzmann factors of 0.05 or more at 25 C).

Defect site	OH mode (cm^{-1})	Ho mode (cm^{-1})	25 ˚C Boltzmann Factor
H_{A2}	N/A	1198.1	1.00
H_{K2}	3316.3	N/A	1.02E-24
H_{D3}	3171.7	N/A	5.01E-25
H_{M2}	3287.1	N/A	4.06E-25
H_{E4}	3242.5	N/A	6.75E-26
H_{G3}	3118.6	N/A	2.35E-26
H_{J4}	3454.8	N/A	2.09E-27
H_{B2}	3330.9	N/A	1.78E-27
H_{I3}	3339.5	N/A	1.40E-27
H_{H3}	3383.5	N/A	1.04E-27
Defect sites	**OH mode (cm^{-1})**	**Ho mode (cm^{-1})**	**25 ˚C Boltzmann Factor**
H_{A2}, H_{M2}	3270.3	1201.5	1.000
H_{A2}, H_{E4}	3251.4	1239.7	0.715
H_{A2}, H_{K2}	3298.8	1243.1	0.700
H_{A2}, H_{G3}	3151.3	1212.5	0.465
H_{A2}, H_{D3}	3130.8	1211.3	0.408
H_{A2}, H_{F3}	3295.7	1220.0	0.131
H_{A2}, H_{I3}	3238.6	1210.2	0.112
H_{A2}, H_{J3}	3259.3	1197.9	0.065
H_{A2}, H_{H4}	3267.7	1196.0	0.051
H_{A2}, H_{J4}	3364.9	1217.9	0.047
H_{A2}, H_{B2}	3255.4	1216.7	0.027
H_{A2}, H_{D4}	3279.4	1224.6	5.81E-03
H_{A2}, H_{G4}	3231.5	1214.7	5.47E-03
H_{A2}, H_{L2}	3194.7	1503.0	9.74E-05
H_{A2}, H_{N2}	3188.8	1328.2	5.03E-05

H_{A2}, H_{C2}	3088.3	1301.7	1.00E-05
Defect sites	**OH mode 1 (cm^{-1})**	**OH mode 2 (cm^{-1})**	**25 ˚C Boltzmann Factor**
H_{D3}, H_{G3}	2798.5	3003.0	8.42E-28

Defect sites	**OH mode (cm^{-1})**	**25 ˚C Boltzmann Factor**
H_{K2}, H_{M2}	3370.2	1.21E-48

Additional commentary on the relation between d(OH···O) and OH frequencies

Figure S9 compares our predicted OH stretching frequencies and hydrogen bonding distances to the relation derived by Libowitzky et al. (1999). Although the trends are generally similar (longer bonding distances correspond to higher wavenumber vibrations), the behavior of our calculated modes deviates somewhat from the experimental observations. These systemic errors in the OH modes may arise from the PBE level of DFT. Although the energies of the vibrational modes we report here are likely close to their true values (within ~100 cm^{-1}), we suggest that these calculations may lack the accuracy required to confidently identify defects contributing to specific vibrational modes.

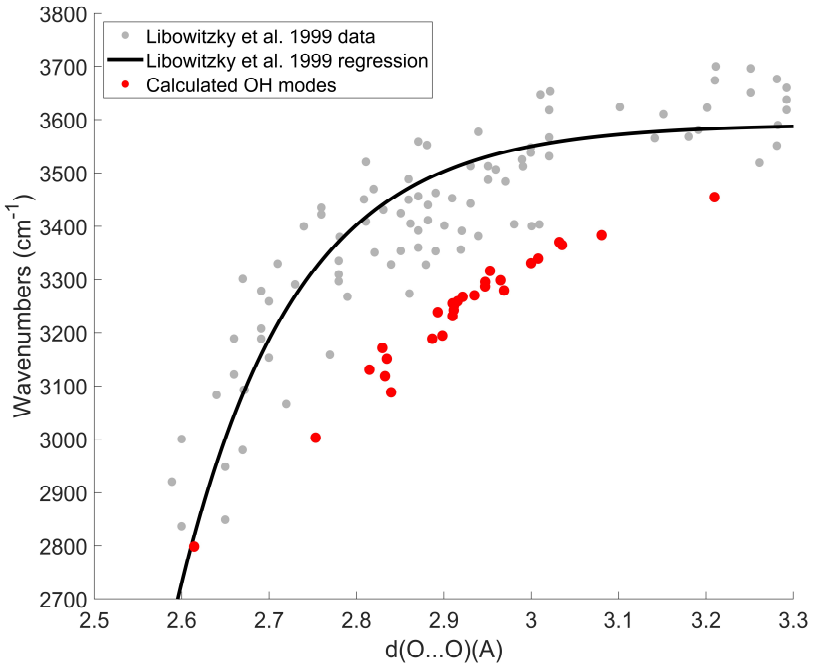

Figure S9. Plot of hydrogen bonding distance (d(OH···O)) versus DFPT-calculated OH stretching frequencies for both 1H and 2H defects (red) compared to the survey data and regression curve from Libowitzky et al., 1999 (gray and black, respectively). Although the two datasets show similar trends, the DFPT calculated modes generally lie outside the experimental data scatter, suggesting a possible underestimation of frequency for given d(OH···O) values.

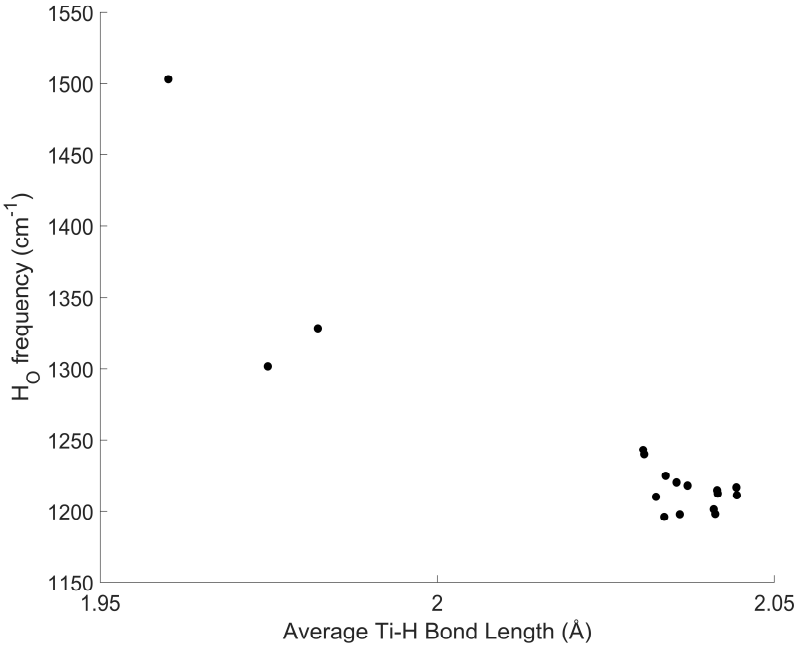

Figure S10. Plot of average Ti-H distance versus DFPT-calculated HO stretching frequencies. Although most of the HO frequencies are clustered in a narrow range of Ti-H distances, expanding the plot to include unusually short Ti-H lengths reveals the response of HO frequencies to bonding lengths. The overall relation mimics trends observed in other types of bonds, further supporting the possibility of H bonded to Ti.

Details on the calculation of heat of formation energies

We estimated the heats of formation for the defect structures using the total energies calculated from the minimized defect structures in addition to the total energies corresponding to the minimized structures of a perfect rutile cell (denoted below as TiO_2), a rutile cell with a single oxygen vacancy (denoted below as TiO_x), a single H_2 molecule, and a single H_2O molecule. H_2O and H_2 were used in favor of O_2 to avoid errors inherent to the PBE description of triplet O_2. The heats of formation for each defect type were calculated as follows:

O vacancy:

$$\Delta H_f = \left(E_{TiO_x} + E_{H_2O}\right) - \left(E_{TiO_2} + E_{H_2}\right)$$

O vacancy, one H:

$$\Delta H_f = \left(E_{TiO_xH} + E_{H_2O}\right) - \left(E_{TiO_2} + \frac{3}{2}E_{H_2}\right)$$

O vacancy, two H:

$$\Delta H_f = \left(E_{TiO_xH_2} + E_{H_2O}\right) - \left(E_{TiO_2} + 2E_{H_2}\right)$$

These values were then adjusted for the heat of formation of O_2 in H_2O, which we calculated from NIST thermochemistry data of -2.506 eV. The other total energy values used in the calculations above are presented below:

Perfect rutile crystal: -437.83 eV

Rutile crystal with one O vacancy: -427.61 eV

H_2O gas molecule: -14.22 eV

H_2 gas molecule: -6.77 eV

Accuracy of PBE-D3 level of DFT

We have used PBE-D3 for a number of catalysis and electrocatalysis experiments for which we have excellent agreement with experiment. For example:

Oxygen evolution reaction over catalytic single-site Co in a well-defined brookite TiO_2 nanorod surface. C. Liu, J. Qian, Y. Ye, H. Zhou, C.-J. Sun, C. Sheehan, Z. Zhang, G. Wan, Y.-S. Liu, J. Guo, S. Li, H. Shin, S. Hwang, T.B. Gunnoe, W.A. Goddard III and S. Zhang. Nat. Catal. **4** (1):36–45 (2021) DOI: 10.1038/s41929-020-00550-5

Reaction mechanism and kinetics for ammonia synthesis on the Fe(111) Surface. J. Qian; Q. An; A. Fortunelli; R.J. Nielsen & W.A. Goddard III. J. Am. Chem. Soc. **140** (20):6288–6297 (2018) DOI:10.1021/jacs.7b13409

Both papers do full kinetics to obtain the TOF. The agreement with experimental rates indicating accuracy better than 0.05 eV.